Submitted to

Europhysics Conference on High Energy Physics, EPS2007, July 19-25, 2007, Manchester
Abstract: **370**
Parallel Session **Strong Interactions**

Electronic Access: www-h1.desy.de/h1/www/publications/conf/conf_list.html

Measurement of Isolated Photon Production in Deep-Inelastic Scattering at HERA

H1 Collaboration

Abstract

The production of isolated photons in deep-inelastic scattering $ep \to e+\gamma+X$ is measured with the H1 detector at HERA. The measurement is performed in the kinematic range of negative four-momentum transfer squared $4 < Q^2 < 150$ GeV^2 and a mass of the hadronic system $W_X > 50$ GeV. The analysis is based on a total integrated luminosity of 227 pb^{-1}. The production cross section of isolated photons with a transverse energy in the range $3 < E_T^\gamma < 10$ GeV and pseudorapidity range $-1.2 < \eta^\gamma < 1.8$ is measured as a function of E_T^γ, η^γ and Q^2. Isolated photon cross sections are also measured for events with no jets or at least one hadronic jet. The measurements are compared with predictions from MC generators modelling the photon radiation from the quark and the electron lines, as well as with calculations at leading and next to leading order in the strong coupling. The predictions significantly underestimate the measured cross sections.

1 Introduction

Isolated photons originating from the hard interaction in high energy collisions are a sensitive probe for precision tests of perturbative QCD, as the photons are largely insensitive to the effects of hadronisation. A good understanding of the standard model production mechanism of isolated photons is important for new physics searches.

Isolated photon[1] cross sections have been measured at various experiments and triggered theoretical discussions [1, 2]. Cross sections measured in fixed target pN experiments (e.g. [3]) show a steeper decrease with the photons transverse momentum, P_T^γ, than predicted by next-to-leading order (NLO) predictions. The CDF [4] and D0 [5] experiments at the Tevatron measured the isolated photon production cross section in $p\bar{p}$ collisions. Whereas D0 finds good agreement with a NLO QCD calculation, the CDF data show again a somewhat steeper P_T^γ dependence than predicted. At HERA prompt photon cross sections have been measured by H1 and ZEUS [6–8] for photoproduction processes ($Q^2 \simeq 0$ GeV^2) and showed reasonable agreement with NLO calculations. An analysis of the isolated photon cross section in deep-inelastic scattering (DIS) with Q^2 larger than 35 GeV^2 has been published by ZEUS [9].

The measurement of isolated photons in DIS provides a test of perturbative QCD in a kinematic range with two hard scales, the negative four-momentum transfer squared Q^2 of the exchanged virtual photon and the transverse energy of the emitted photon E_T^γ. In contrast to photoproduction, the measurement of isolated photons in DIS has less uncertainties from contributions of resolved photon processes. Isolated photons in DIS are produced at lowest order ($\alpha^3\alpha_s^0$) as shown in figure 1. Already at this order a jet is expected in the hadronic final state besides the proton remnant jet due to the electron recoil.

The final state photon may be emitted by a quark (QQ) and by wide angle radiation from the lepton (LL). The interference contribution (LQ) is expected to be small. fraction. Since the photon and the scattered electron are well separated in the present analysis, low angle QED radiation is suppressed. The QQ contribution has two different origins: the direct radiation of a photon from the quark and the fragmentation of a hadronic jet into a photon carrying a large fraction of the jet energy. This process is described by a process-independent quark-to-photon fragmentation function, which can not be calculated perturbatively. Theoretical calculations encounter already at leading order (LO) an infrared singularity due to the emission of a photon collinear to the quark. This makes a NLO prediction for the inclusive cross section considerably involved. The contributions from the collinear singularity and the quark-to-photon fragmentation can not be eliminated but are suppressed by the isolation requirement for the photon.

This paper presents the measurement of isolated photon production $e + p \rightarrow e + \gamma + X$. Jet production is also investigated. Isolated photons with transverse energy $3 < E_T^\gamma < 10$ GeV and pseudorapidity $-1.2 < \eta^\gamma < 1.8$ are selected in DIS events in the kinematic regime $4 < Q^2 < 150$ GeV^2, inelasticity $y > 0.05$ and a mass of the hadronic system $W_X > 50$ GeV. The measurement range covered by this analysis significantly extends the kinematic range probed by the previous measurement [9]. Photons are identified by a multivariate analysis of the shapes of the calorimeter energy deposits, separating the photons from neutral hadrons and their decay

[1]Photons coupling to the interacting partons are often called "prompt" in contrast to photons from hadron decays or photons emitted by leptons.

products. The results are compared to a recent leading order, $\mathcal{O}(\alpha^3\alpha_s^0)$, calculation [10, 11] and to predictions of the Monte Carlo (MC) models PYTHIA [12], simulating the QQ process, and RAPGAP [13] for the LL process. The cross sections for a photon plus at least one jet are further compared to a NLO calculation [14].

2 H1 Detector

A detailed description of the H1 detector can be found in [15]. In the following, only detector components relevant to this analysis are briefly discussed. The origin of the H1 coordinate system is the nominal ep interaction point, with the direction of the proton beam defining the positive z-axis (forward direction). Transverse momenta are measured in the $x - y$ plane. Polar (θ) and azimuthal (ϕ) angles are measured with respect to this reference system. The pseudorapidity is defined to be $\eta = -\ln\tan(\theta/2)$.

In the central region ($25^\circ < \theta < 165^\circ$) the interaction region is surrounded by the central tracking system, which consists of a silicon vertex detector, drift chambers and multi-wire proportional chambers, all located within a solenoidal magnetic field of 1.16 T. The trajectories of charged particles are measured in the range $-1.7 < \eta < 1.7$ with a transverse momentum resolution of $\sigma(P_T)/P_T \simeq 0.005\,P_T\,/\mathrm{GeV} \oplus 0.015$. The Forward Tracking Detector ($7^\circ < \theta < 25^\circ$) and the Backward Drift Chamber (BDC, operated in 1999-2000) or Backward Proportional Chambers (BPC, for 2003-2005) provide track segments of charged particles at smaller and larger θ than the central tracker, respectively.

The liquid argon (LAr) sampling calorimeter surrounds the tracking chambers and has an asymmetric polar angle coverage of $4^\circ < \theta < 154^\circ$ and full azimuthal acceptance. It consists of an inner electromagnetic section with lead absorbers and an outer hadronic section with steel absorbers. The calorimeter is divided into eight wheels [16] along the beam axis, each of them segmented in ϕ into eight modules, separated by small regions of inactive material. The electromagnetic and the hadronic sections are highly segmented in the transverse and the longitudinal direction with about $44\,000$ cells in total; the granularity is larger in the electromagnetic part and increasing in the forward part. For particles coming from the ep interaction region, the laterally projected cell size in the electromagnetic part varies between 5×5 cm^2 in the forward and at most 7×13 cm^2 in the central region. The longitudinal segmentation in the different wheels varies from three (central) to four (forward) layers in the electromagnetic and from four to six in the hadronic section. The first electromagnetic layer has a thickness of about 3 to 6 radiation lengths for particles coming from the interaction region. Electromagnetic shower energies are measured with a precision of $\sigma(E)/E = 12\%/\sqrt{E/\,\mathrm{GeV}} \oplus 1\%$ and hadronic energies with $\sigma(E)/E = 50\%/\sqrt{E/\,\mathrm{GeV}} \oplus 2\%$ as determined in test beam experiments [17, 18].

In the backward region $153^\circ < \theta < 178^\circ$, the particle energies are measured by a lead-scintillating fibre spaghetti calorimeter (SpaCal) [19].

The luminosity is determined from the rate of the Bethe-Heitler process $ep \rightarrow ep\gamma$, measured using a photon detector located close to the beam pipe at $z = -103$ m, in the backward direction.

DIS events at Q^2 values up to 150 GeV^2 are triggered by the energy deposition of the scattered electron in the SpaCal. For particles entering the SpaCal at low radii, the SpaCal trigger is combined with a tracking requirement in the central detector [20, 21] and a signal from the central proportional chambers [22–24]. The trigger efficiency for DIS events containing an electron with an energy above 10 GeV is greater than 98%.

3 Monte Carlo Simulations

MC simulations are used to correct the data for detector acceptances, inefficiencies and migrations and to compare the measured cross sections with Monte Carlo model predictions.

The two generators PYTHIA and RAPGAP are used to generate events with photons produced in the hard interaction. PYTHIA simulates such photons through radiation from the struck quark (QQ). Photon radiation by the electron (LL) is simulated by RAPGAP (RAPGAP rad.). The small contribution from interference [10] is neglected. Both generators are based on LO QCD matrix elements. Higher order QCD radiation is modelled using initial and final state parton showers in the leading log approximation [25]. Fragmentation into hadrons is simulated using the LUND string fragmentation model [26] as implemented in JETSET [27]. The simulation uses the CTEQ6L proton parton densities [28].

The combination of the signal predictions of the two MCs is not able to describe the measured cross section. The cross sections are found to be reasonably described if PYTHIA is scaled by a factor 2.3 and RAPGAP is not scaled. This combined “scaled signal MC” is used to correct the data, whereas the unscaled MC prediction (“signal MC”) is compared to cross section measurements.

As an alternative, the HERWIG [29] generator is used to model the signal from the QQ subprocess. HERWIG simulates the fragmentation into hadrons through the decay of colourless parton clusters and uses the equivalent-photon approximation for the incoming photon beam. Isolated photon production in DIS is derived approximately as Compton scattering between the photon and a quark. This approximation is not valid for Q^2 above a few GeV^2, therefore HERWIG is only used to estimate the systematic uncertainties due to the fragmentation model.

The main background is due to photons produced in hadron decays in DIS events. It is modelled using the RAPGAP generator, with initial and final state radiation switched off (RAPGAP non-rad.).

The shower shape analysis described in section 5 requires high statistics samples of shower simulations in the whole phase space of energy and pseudorapidity. For this purpose the calorimeter signals produced by single photons and photons from decays of single neutral particles (”single particle events”) are simulated.

All generated events are passed through a full GEANT [30] simulation of the H1 detector and through the same reconstruction and analysis program as used for the data.

4 Event Selection

The event sample used in this analysis was collected with the H1 Detector at HERA in the period from 1999 to 2005 at a centre-of-mass energy of 318 GeV. The corresponding integrated luminosity is 227 pb^{-1}. In a first step, DIS events are selected with the scattered electron[2] measured in the SpaCal. In a second step events with an isolated photon candidate in the LAr calorimeter are selected. The isolation requirement largely suppresses background from photons produced in hadron decays.

4.1 Selection of DIS events

DIS events are selected with the scattered electron identified by a compact electromagnetic cluster [31] with an energy $E_e' > 10$ GeV and a polar angle $\theta_e < 177^\circ$ in the SpaCal. Matching signals in the backward tracking chambers are required for electron candidates with $E_e' < 18$ GeV. The scattering angle of the electron is determined from the measured impact position in the backward tracking chamber and the position of the energy cluster in the SpaCal together with the reconstructed primary vertex.

Background from events at low Q^2, in which the electron escapes through the beam pipe and a hadron fakes the electron signature, is suppressed by the requirement that the difference $\Sigma(E - p_z)$ between the total energy and the longitudinal momentum be in the range $35 < \Sigma(E - p_z) < 70$ GeV, where the sum includes all hadronic final state particles and the scattered electron.

Non-ep background is removed by restricting the z-coordinate of the event vertex to be within ± 40 cm of the average interaction vertex position and requiring at least one good track in the central tracking system with polar angle $30^\circ < \theta < 150^\circ$ not associated to the electron.

The energy E_e' and polar angle θ_e of the scattered electron candidate are used to reconstruct y and Q^2 according to $Q^2 = 2\, E_e E_e'(1 + \cos\theta_e)$ and $y = 1 - E_e'/(2E_e)(1 - \cos\theta_e)$, where E_e is the electron beam energy. The analysis covers the kinematic region $4 < Q^2 < 150$ GeV^2 and $y > 0.05$.

4.2 Selection of isolated photon candidates and jets

Photon candidates are identified as clusters in the electromagnetic section of the LAr calorimeter with a transverse energy $3 < E_T^\gamma < 10$ GeV and pseudorapidity $-1.2 < \eta^\gamma < 1.8$ in the H1 laboratory frame.

Photon candidates are rejected if they are close to inactive regions between calorimeter modules [16] or if a track geometrically matches the electromagnetic cluster with a distance of closest approach to the cluster's barycentre of less than 20 cm. Neutral hadrons that decay into multiple photons, predominantly $\pi^0 \to \gamma\gamma$, constitute the main background. In most cases

[2]The analysis uses data from periods when the beam lepton was either a positron or an electron. Unless otherwise stated, this paper uses the term electron generically to refer to both the electron and the positron.

such decay photons are merged into one electromagnetic cluster, which tends to have a wider transverse distribution than that of a single photon. Therefore, a cut is applied on the transverse radius[3] of the photon candidate cluster of $R_T < 6$ cm. In addition, the invariant mass of the cluster, when combined with the closest neighbouring electromagnetic cluster having an energy above 80 MeV, must be larger than 300 MeV. This requirement rejects candidates that originate from π^0 decays with two photons reconstructed in separate clusters. Only events with exactly one photon candidate are accepted. Less than 1% of the events are rejected because more than one photon candidate is found.

The mass of the final state hadronic system is reconstructed using the four-momenta of the incoming electron (p_e) and proton (p_p), the scattered electron (p'_e) and the photon candidate (p_γ) as $W_X = \sqrt{(p_e + p_p - p'_e - p_\gamma)^2}$. The contribution from elastic Compton scattering ($p + e \rightarrow p + e + \gamma$) is suppressed by requiring that the invariant mass of the hadronic system be $W_X > 50$ GeV.

Final state hadrons are reconstructed from deposits in the LAr calorimeter in combination with tracking information. Following the so-called "democratic" procedure [32, 33], the photon candidate and the reconstructed hadrons in each event, are combined into jets using the k_T algorithm [34], where jets are treated as massless. The algorithm is used with a P_T-weighted recombination scheme and the separation parameter R_0 is set to 1. Jets are selected with a transverse momentum of $P_T^{jet} > 2.5$ GeV and a pseudorapidity in the range $-2.0 < \eta^{jet} < 2.1$. Due to the harder kinematical cuts for the photon candidate there is always a jet containing the photon candidate, called the photon-jet. All other jets classify as hadronic jets. For hadronic jets the η^{jet}-range is restricted to $-1.0 < \eta^{jet} < 2.1$. The hadronic jets are found to be well correlated to the partonic jets even at low transverse energies. To ensure isolation of the photon, the fraction z of the transverse energy of the photon-jet carried by the photon candidate has to be larger than 90%. This definition of the isolation requirement is stable against infrared divergences and thus well-suited for comparisons with perturbative QCD calculations.

The distribution of the transverse energy and polar angle of the isolated photon candidates is shown in figure 2 together with the MC predictions for the scaled signal and the background. The sum of the MCs describes the data well.

Events with either no hadronic jet or at least one hadronic jet are called "photon plus no-jets" and "photon plus jet", respectively. The P_T^{jet} and θ^{jet} distributions for the hadronic jet with the largest transverse momentum are shown in figure 3. Both distributions are reasonably well described by the sum of the scaled signal and background MCs.

In total 14670 events with a scattered electron and an isolated photon candidate are selected, out of which 6495 have at least one additional hadronic jet.

5 Photon Signal Extraction

5.1 Shower shape analysis

The extraction of the photon signal exploits the fine granularity of the electromagnetic part of the LAr calorimeter. In order to discriminate between signal photons and the background from

[3]For a definition of the transverse radius see section 5.

neutral hadrons and their decay products, the calorimeter cluster corresponding to the isolated photon candidate is further analysed using the following six shower shape variables [35]:

1. The fraction of the energy of the electromagnetic cluster contained in the cell with the largest energy deposit ("hottest" cell).
2. The fraction of the energy of the electromagnetic cluster contained in four or eight (depending on the granularity of the calorimeter) contiguous cells in the first two calorimeter layers. The cells include the hottest cell and are chosen to maximise the energy which they contain ("hot core"). Both, this and the first variable are sensitive to the compactness of the cluster in the calorimeter.
3. The fraction of the cluster's energy detected in the first calorimeter layer ("layer1"), which is expected to be larger on average for multi-photon clusters than for those initiated by a single photon.
4. The transverse[4] symmetry S_T of a cluster defined as the ratio of the spread (defined by root mean squared) of the transverse cell distributions along the two principal axes. A photon cluster is expected to have a symmetric cluster, whereas multi-photon clusters are typically more asymmetric.
5. The transverse radius of the cluster defined as the square root of the second central transverse moment $R_T = \sqrt{\mu_2}$, where the k'th central tranverse moment of the cell distribution is given by $\mu_k = \langle|\vec{r} - \langle\vec{r}\rangle|^k\rangle$. $\vec{r}$ is the transverse projection of the transverse cell positions and $\langle\vec{r}\rangle = (\sum_{i=0}^{n} E_i\vec{r_i})/\sum E_i$ the energy weighted average of the cell positions $\vec{r_i}$.
6. The transverse kurtosis K_T defined as the ratio of the fourth and squared second moment of the transverse energy distribution of the cluster cells $K_T = \mu_4/(\mu_2)^2 - 3$, which specifies how strongly the energy distribution is peaked. For a Gaussian distribution K_T equals zero.

The discrimination power of signal and background becomes weaker at high transverse energies, where the multi-photon clusters become more similar to a single photon cluster. Therefore events with $E_T^\gamma > 10$ GeV are excluded from the measurement as presented in section 4.2.

The six shower shape variables are shown for the isolated photon candidates in figure 4. The measured distributions are compared with the sum of the background and the scaled signal MC distributions. A good agreement is observed.

5.2 Signal extraction

In order to discriminate between single photons (signal) and single neutral hadrons (background), probability density functions are determined for the six shower shape variables, using simulated "single particles events" (see section 3) with photons and a mix of neutral hadrons

[4]In the context of the cluster shape analysis the transverse plane is here defined as perpendicular to the direction of the incoming particle.

(π^0, η, η', ρ, ω, $K^\star$, K_L^0, K_S^0, n and $\bar{n}$), respectively. The relative contributions of the neutral hadrons are taken from the RAPGAP MC. Though the main contribution comes from π^0 and η (roughly 90%), there is still a sizeable contribution from the other neutral particles.

The single particle simulation is corrected for overlap effects that can occur in a hadronic environment, which affect the cluster shapes. The cluster overlap is found to be important only in the description of the background. The overlap leads to a loss of photon candidates due to the distortion of the transverse cluster radius, which then exceeds in most cases the upper limit of 6 cm required in the analysis (cf. section 4.2). This loss is modelled using a probability p_{co} for cluster overlap proportional to the transverse area of the cluster $p_{co} = a \cdot R_T^2$ with $a = 0.004\,\mathrm{cm}^2$. The constant a is determined by a comparison with full event MCs in phasespace regions where sufficient statistics are available.

The multi-dimensional photon and background probability densities are taken as the product of the respective shower shape densities. For each event a discriminator (D) is formed, which is defined as the photon probability density divided by the sum of the probability densities for photons and background. The discriminator produces in general larger values for isolated photons than for the decay photons. Figure 5 shows the discriminator distribution for the data together with the predictions of the background and the scaled signal MC. The data are nicely described by the sum of the MC predictions.

Since the shower shape densities vary significantly with E_T^γ and η^γ, the discriminator is determined in analysis bins in (E_T^γ, η^γ), with three bins in E_T^γ and five bins in η^γ. The bins in η^γ correspond to different wheels of the calorimeter. The contribution of photons and neutral hadrons in any of the 15 analysis bins is determined by independent minimum-χ^2 fits of the signal and background discriminator distributions to the data distribution separately for the inclusive sample, photon plus no-jets and photon plus jet . The χ^2 function is defined to be

$$\chi^2 = \sum_i \frac{\left(N_{data,i} - X_{bg} n_{bg,i} - X_{sig} n_{sig,i}\right)^2}{\sigma^2_{data,i} + X^2_{bg}\,\sigma^2_{bg,i} + X^2_{sig}\,\sigma^2_{sig,i}}$$

where the sum runs over the bins of the discriminator distributions. $N_{data,i}$ is the number of data events in the i'th bin. $n_{sig,i}$ and $n_{bg,i}$ denote the i'th bin content of the signal and background discriminator distribution, respectively, normalised to unity. The σ_i represent the associated statistical errors. X_{sig} and X_{bg}, representing the number of signal and background events, respectively, are the parameters that are determined by the fit. If the content in any histogram bin is small ($N_{data,i} < 7$), adjacent bins are merged. The fit quality is acceptable in all differential bins.

The total number of isolated photons is obtained by summing X_{sig} in all analysis bins. As a result 4372 ± 145 signal events are attributed to the inclusive data sample. In the photon plus no-jets and photon plus jet subsamples 1755 ± 106 and 2606 ± 95 signal events are found, respectively. This implies a signal fraction in the selected inclusive sample described in section 4.2 of 29%. The signal fraction is 20% for the photon plus no-jets and 39% for the photon plus jet sample, showing that the jet multiplicity for events with isolated photons is higher than for background events.

5.3 Cross section determination

In each bin of the kinematic variables, the cross section σ is computed from the number of events with photons in the corresponding bin as $\sigma = X_{sig}/(\mathcal{L} \cdot \epsilon)$, where $\mathcal{L}$ is the luminosity. The correction factor ϵ takes into account the acceptance, trigger and reconstruction efficiencies and migration between the bins. It is calculated using the scaled signal MC. Bin averaged cross sections are quoted in all tables and figures.

The total inclusive cross section is obtained by summing the results in all analysis bins. The cross sections $d\sigma/dE_T^\gamma$ and $d\sigma/d\eta^\gamma$ are obtained accordingly by summing all corresponding bins in η^γ and E_T^γ, respectively. The Q^2 dependence of the cross section is determined by fitting the discriminator distribution in five different bins in Q^2. In these fits, the discriminator distributions of the signal and background single particles for different bins in the E_T^γ, η^γ-grid are combined as to follow the E_T^γ and η^γ dependence measured in the entire Q^2 range. Variations of the Q^2 dependence within uncertainties have a negligible effect.

6 Systematic Uncertainties

Two additional event samples are used in the determination of systematic errors and in-situ energy calibration. The first sample, containing Bethe Heitler events, $ep \to e\gamma p$, consists of events with an electron reconstructed in the LAr calorimeter, a photon in the SpaCal and nothing else in the detector. The second (complementary) sample is selected by requiring an electron in the SpaCal and a photon in the LAr calorimeter. Such events originate to a large part from deeply virtual Compton scattering $ep \to e\gamma p$. These selections, denoted BH and DVCS, respectively, are independent of the main selection for isolated photons and provide a clean sample of electromagnetic clusters in the LAr calorimeter.

The effects of the different systematic errors on the cross section is evaluated by applying variations to the MC simulation.

The following uncertainties are considered:

- The measured shower shapes in the BH and DVCS event samples are compared to simulated single particle photons and electrons, respectively. The uncertainty is estimated by distorting the simulated shower shapes within limits set by the BH and DVCS measurements. The fits for the signal extraction (section 5.2) are repeated with the distorted input distributions. The resulting systematic errors are between 11% and 25% for the single differential cross sections. The error increases with increasing E_T^γ and towards large η^γ and is independent of Q^2.
- The photon energy reconstruction is checked with the BH and DVCS events. For the BH events the cluster transverse energy is compared with the track measurement. For DVCS events, the energy of the cluster is compared to the energy calculated using the double angle method [36]. The photon energy scale uncertainty estimated with this method varies from 1% for photons detected in the backward region to 4% for forward photons. The resulting error on the total inclusive cross section is $+3.6\%$ and -2.6%.

- An uncertainty of 3 mrad (4 mrad for $\eta_\gamma > 1.4$) is attributed to the measurement of the polar angle of the photon. This uncertainty is found by comparing the angular measurements of the track and the cluster for BH electrons. The resulting error on the total inclusive cross section is $+0.1\%$ and -0.7%.

- An uncertainty of up to 2% is attributed to the energy of the scattered electron and an uncertainty of 2 mrad to the measurement of the scattering angle. The resulting error on the total inclusive cross section is $+1.9\%$ and -2.9%.

- A 3% uncertainty is attributed to the energy of hadronic final state objects [37]. This affects the total cross section by $+1.2\%$ and -0.7%.

- A 5% uncertainty is applied for the correction of the cluster overlap which corresponds to half the size of the correction.

- The model dependence of the acceptance corrections is derived by PYTHIA and HERWIG simulations. A resulting error of 5% is found for the inclusive and the photon plus jet and 10% for the photon plus no-jets cross sections.

- The uncertainty of the ratio of the LL and QQ contributions for the acceptance corrections is taken into account by varying the scaling factor for PYTHIA from 1.5 to 3. For the double differential cross section, a maximum systematic error of 5% is found. In regions with $\eta^\gamma > -0.6$, the systematic error is below 1%.

- An uncertainty of 1% in the description of the trigger efficiency by the simulations is included in the systematic error.

- The uncertainty on the track reconstruction efficiency results in an error of $\pm0.3\%$ for the total inclusive cross section.

- The uncertainty on the conversion probability of the photons before entering the calorimeter results in a systematic error of 2% of the cross sections.

- The uncertainty on the luminosity measurement is 2%.

In each analysis bin the individual effects of these experimental uncertainties are combined in quadrature. The systematic uncertainty obtained on the total inclusive cross section is $+13.6\%$ and -15.5%. The largest contribution to this uncertainty arises from the systematic effect attributed to the description of the shower shapes, which is partly correlated among measurement bins.

7 Theoretical Predictions

The measured cross sections are compared to the unscaled MC prediction as discussed in section 3 and to a LO, $\mathcal{O}(\alpha^3\alpha_s^0)$, QCD calculation [10, 11]. The photon plus jet cross sections are further compared to a next-to-leading order (NLO), $\mathcal{O}(\alpha^3\alpha_s)$, calculation [14] which is not available for the inclusive nor for the photon plus no-jets measurement. The cross section $\sigma(ep \to e\gamma X)$ is calculated by convoluting the parton-level lepton-quark cross sections $\hat{\sigma}(eq \to e\gamma q)$ with the parton density functions of the quarks in the proton. In the scattering amplitudes, the lepton-quark interaction is mediated by the exchange of a virtual photon with four-momentum transfer squared Q^2 and the final state photon is emitted by the lepton or the quark.

The QQ contribution is dominated by the direct radiation of the photon from the quark involved in the parton level process, but also contains the contribution from quark fragmentation to a photon [38, 39]. While the direct part can be calculated in perturbation theory, the fragmentation contribution has to be determined from data. It is described by a process-independent quark-to-photon fragmentation function $D_{q\to\gamma}(z)$ where z is the fraction of the quark's momentum carried by the photon. Even at leading order, the parton-level cross section contains a collinear quark-photon divergence, which is factorised into the fragmentation function at a factorisation scale $\mu_{F,\gamma}$.

So far only two measurements exist that give direct information on the quark-to-photon fragmentation function. These measurements were made by the LEP experiments ALEPH [33] and OPAL [40]. Only the ALEPH measurement has the precision to allow a determination of $D_{q\to\gamma}(z)$. The LO calculation used in this analysis is based on the ALEPH LO parametrisation of $D_{q\to\gamma}(z)$ [32, 33]. The NLO calculation uses the fragmentation function from Bourhis, Fontannaz and Guillet [41]. In the MC models the contribution from fragmentation is not included.

For photons plus no-jets the quark-to-photon fragmentation enters already at lowest order ($\alpha^3\alpha_s^0$) [11], in contrast to the photon plus jet sample where the fragmentation contribution is of the order $\alpha^3\alpha_s^1$, giving the photon plus no-jets sample particular interest.

In the LL subprocess, the photon is radiated by the lepton. The reconstruction of the photon and the electron in different parts of the detector ensures that the two particles are separated, hence the LL term contains no collinear singularities. The interference term (LQ), which differs in sign for e^+p and e^-p scattering, is included in the calculations. It contributes less than 3% to the cross section [10].

The NLO calculation of the photon plus jet cross sections includes processes with an additional gluon, either as the incoming parton or in the final state, as well as virtual corrections. The renormalisation and factorisation scales are fixed by $\mu_R = \sqrt{Q^2 + (P_T^{jet})^2}$ and $\mu_F = \sqrt{Q^2 + (P_T^{jet})^2}$. Theoretical uncertainties are obtained from varying μ_R and μ_F independently by a factor two up and down. These uncertainties are small and lower than the uncertainties from the choice of the PDF parametrisation.

The calculations of the isolated photon cross section are made for the same ratio of luminosities for e^+p (52.1%) and e^-p (47.9%) scattering as the data. The cuts in the theoretical calculations are adjusted to correspond to the experimental cuts described in this paper and the calculations are based on the same jet algorithm as used in this analysis. The CTEQ6L [28] leading order parametrisation of proton parton distributions is used. Different proton parton density functions are found to change the predictions by $5 - 10\%$. The LO and NLO predictions are compared to the data after a correction for hadronisation effects. The correction factors

f_{had} are defined as the ratio of the cross sections calculated from hadrons to those from partons and are determined from the scaled signal MC. The uncertainty of the correction factor is estimated by comparing the correction factors obtained from PYTHIA with those from HERWIG. The corrections are at most -30% and the uncertainty is 5%.

8 Results

The cross sections presented below are given for the phase space defined in table 1. The differential cross sections are compared with the signal MC predictions (unscaled PYTHIA plus RAPGAP) and LO and NLO calculations.

8.1 Inclusive isolated photon cross sections

The measured inclusive isolated photon cross section is

$$\sigma(ep \rightarrow e\gamma X) = 50.3 \pm 1.7 \text{ (stat) } {}^{+6.8}_{-7.8} \text{ (syst) pb.}$$

The LO calculation predicts a cross section of 28.2 pb, while the signal MC expectation is 26.4 pb. Both predictions significantly underestimate the total inclusive cross section by almost a factor of two.

Bin averaged differential cross sections $d\sigma/dE_T^\gamma$, $d\sigma/d\eta^\gamma$ and $d\sigma/dQ^2$ are presented in table 2 and in figure 6. For all measurement bins the total uncertainty is dominated by systematics. The measurements are compared to the predictions by the signal MC and the LO calculation. The correction factor f_{had} for the correction of the LO calculation to hadron level is listed in all the cross section tables.

The LO calculation lies furthest below the data at low Q^2. It provides a reasonable description of the shapes of the data distributions in E_T^γ and η^γ, with some tendency to lie further below the data at high transverse energies and central and backward rapidities of the photon. The LL and QQ contributions are shown separately in figure 6. Their relative contributions depend strongly on η^γ and Q^2. At backward η^γ, close to the scattered electron, the LL contribution is of similar magnitude to that of QQ. At forward and central η^γ, radiation by the quark dominates. The interference contribution LQ is included in the sum, but not shown separately as it amounts to a few percent of the total cross section only.

The cross section predicted by the signal MC agrees reasonably well with the LO calculation. The PYTHIA prediction follows the shape of the QQ contribution, whereas the RAPGAP prediction follows the LL contribution. As the comparisons with the data are similar, further comparisons are only shown to the LO calculation.

Figure 7 and table 3 present the E_T^γ dependence of the cross section in five different bins in η^γ, corresponding to the wheel structure of the LAr calorimeter. At backward η^γ, the LL and the QQ terms are of similar magnitude. As the LL term is very small for $\eta^\gamma > -0.6$, the underestimation of the data by the LO calculation by roughly a factor two can be attributed mainly to an underestimated QQ contribution. However, the shape of the distributions is found to be reasonably reproduced.

At $Q^2 > 40\,\mathrm{GeV}^2$, the agreement of the predictions with the data is somewhat better, as can be seen in figure 8 and table 4. The total inclusive cross section for $Q^2 > 40$ GeV^2 is

$$\sigma(ep \rightarrow e\gamma X) = 14.0 \pm 0.8 \text{ (stat) } ^{+2.1}_{-2.1} \text{ (syst) pb.}$$

The LO (10.3 pb) prediction is about 30% below the data. The shapes of the $d\sigma/dE_T^\gamma$ and $d\sigma/d\eta^\gamma$ distributions are well reproduced. According to the prediction the relative contribution of LL is higher than at low Q^2.

The present measurement is extrapolated to the phase space of the analysis performed by the ZEUS collaboration [9] ($Q^2 > 35$ GeV^2, $y > 0$, $E_e' > 10$ GeV, $139.8 < \theta_e < 171.9°$ and $5 < E_T^\gamma < 10$ GeV). The extrapolation is not possible for $\eta^\gamma < -0.6$, because the photon and the electron are not well separated. Figure 9 shows the comparison of the differential cross section $d\sigma/d\eta^\gamma$. A good agreement between the two measurements is observed. In the ZEUS analysis photon radiation from the electron is neglected in the acceptance corrections, and in addition no W_X cut is applied. A rough estimate shows that with the W_X cut used by H1 and the acceptance calculation with the combination of PYTHIA and RAPGAP, the ZEUS cross sections is expected to be lower by about $10 - 30\%$. A different photon isolation criterion is used in the ZEUS analysis which is not corrected for. Studies of isolated photons in photoproduction indicate that the two different isolation criteria give very similar results. The measurement presented in this paper significantly extends the kinematical region probed by ZEUS in transverse energy, pseudorapidity and Q^2.

8.2 Photon plus no-jets and photon plus jet cross sections

The cross section for jet production in association with isolated photons is studied. The measurement is performed in the phase space defined for the inclusive cross section with an additional jet requirement or veto as shown in table 1.

The total cross section for photon plus no-jets is measured as

$$\sigma(ep \rightarrow e\gamma Y) = 18.7 \pm 1.2 \text{ (stat) } ^{+3.3}_{-3.4} \text{ (syst) pb,}$$

where Y contains no accepted hadronic jet. The prediction of the LO calculation is 11.7 pb. The cross section for the photon plus at least one jet is measured as

$$\sigma(ep \rightarrow e\gamma jetX) = 31.6 \pm 1.2 \text{ (stat) } ^{+4.2}_{-4.8}\text{(syst) pb.}$$

The prediction of the LO calculation is 16.7 pb. For both samples the predictions are significantly lower than the data. The observed ratio of data to LO prediction is very similar to the inclusive measurement for both samples. As in the inclusive sample similar conclusions are found for the MC predictions.

A comparison to a NLO calculation is possible for the photon plus jet cross sections. It predicts a cross section for photon plus jet of 20.2 ± 0.6 pb, about 20% higher than the LO prediction but still roughly 35% lower than the data. A higher cut on $P_T^{jet} > 4$ GeV does not significantly improve the description of the data.

Figure 10 and table 5 show the differential cross sections $d\sigma/dE_T^\gamma$, $d\sigma/d\eta^\gamma$ and $d\sigma/dQ^2$ for the photon plus no-jets and photon plus jet selection in comparison with the LO predictions. For both samples the LO prediction describes the shapes of the $d\sigma/dE_T^\gamma$ and $d\sigma/d\eta^\gamma$ distributions reasonably well and is furthest below the data at low Q^2, where the QQ term dominates. All four diagrams in figure 1 contribute to the photon plus no-jets and photon plus jet sample, but the LL contribution is largely suppressed for the photon plus no-jets sample due to the cut on W_X. Since, at leading order, the fragmentation contribution to the cross section enters only the photon plus no-jets sample, the observed excess can not solely be attributed to an underestimation of that contribution. The cross section for photon plus jet production is roughly two times higher than for photon plus no-jets. This is in contrast to the inclusive $ep \to eX$ cross section, where topologies with an additional jet are suppressed by $\mathcal{O}(\alpha_s)$. The above observation reflects the fact that both cross sections have the same order in perturbative QCD.

In addition the differential cross sections $d\sigma/dE_T^\gamma$, $d\sigma/d\eta^\gamma$ and $d\sigma/dQ^2$ for the photon plus jet selection are compared to the NLO prediction. On average, the NLO prediction for the photon plus jet sample is higher than the LO prediction, most significantly at low Q^2, but is still lower than the data by roughly 35%. The shapes of all three distributions are described reasonably well.

9 Conclusions

The cross section for isolated photon production in deep-inelastic scattering has been measured in the kinematic region $4 < Q^2 < 150$ GeV^2, $y > 0.05$ and $W_X > 50$ GeV. Compared to previous measurements the range of Q^2 is extended from $Q^2 > 35$ GeV^2 to $Q^2 > 4$ GeV^2. The cross section receives contributions from photon radiation by the quark (QQ) as well as wide angle bremsstrahlung of the initial and final leptons (LL) and interference.

The data are compared to a LO calculation which underestimates the measured cross section by roughly a factor two. The prediction is most significantly below the data at low Q^2. The shapes of the $d\sigma/dE_T^\gamma$ and $d\sigma/d\eta^\gamma$ distributions are described reasonably well. The cross sections in different bins of η^γ show that, for $\eta^\gamma > -0.6$, where the LL contribution is small, the difference can mainly be attributed to an underestimation of the QQ contribution. The data is further compared to predictions from MC generator PYTHIA for the simulation of photons radiated by the quark together with photons radiated from the electron as predicted by RAPGAP. The MC predictions are very similar to the predictions from the LO calculation and show the largest discrepancy at low Q^2.

Jet production in events with isolated photons is also studied. The cross sections for events with no or at least one hadronic jet are underestimated by the LO prediction by a similar factor as in the inclusive measurement. Again the expectations are furthest below the data at low Q^2. The total photon plus jet cross section is roughly double the photon plus no-jets cross section as expected from the calculations. The NLO prediction for photon plus jet is higher than the LO prediction, most significantly at low Q^2, but still underestimates the data. The NLO calculation describes the shapes of the differential cross sections reasonably well.

The present measurements indicate the need for higher order corrections in the calculation of isolated photon phenomena in deep-inelastic ep scattering.

Acknowledgements

We are grateful to the HERA machine group whose outstanding efforts have made this experiment possible. We thank the engineers and technicians for their work in constructing and maintaining the H1 detector, our funding agencies for financial support, the DESY technical staff for continual assistance and the DESY directorate for support and for the hospitality which they extend to the non DESY members of the collaboration. We would like to thank Aude Gehrmann-De Ridder, Thomas Gehrmann and Eva Poulsen for providing the LO calculations and many helpful discussions and G. Kramer and H. Spiesberger for the NLO calculation.

References

[1] P. Aurenche *et al.*, Phys. Rev. D **73** (2006) 094007 [hep-ph/0602133].

[2] J. Gayler, Acta Phys. Polon. B **37** (2006) 715 [hep-ex/0511035].

[3] L. Apanasevich *et al.* [Fermilab E706 Collaboration], Phys. Rev. D **70** (2004) 092009 [hep-ex/0407011].

[4] F. Abe *et al.* [CDF Collaboration], Phys. Rev. Lett. **73** (1994) 2662 [Erratum-ibid. **74** (1995) 1891];
D. Acosta *et al.* [CDF Collaboration], Phys. Rev. D **65** (2002) 112003 [hep-ex/0201004];
D. Acosta *et al.* [CDF Collaboration], Phys. Rev. D **70** (2004) 074008 [hep-ex/0404022];
D. Acosta *et al.* [CDF Collaboration], Phys. Rev. Lett. **95** (2005) 022003 [hep-ex/0412050].

[5] B. Abbott *et al.* [D0 Collaboration], Phys. Rev. Lett. **84** (2000) 2786 [hep-ex/9912017];
V. M. Abazov *et al.* [D0 Collaboration], Phys. Lett. B **639** (2006) 151 [hep-ex/0511054].

[6] J. Breitweg *et al.* [ZEUS Collaboration], Phys. Lett. B **472** (2000) 175 [hep-ex/9910045].

[7] A. Aktas *et al.* [H1 Collaboration], Eur. Phys. J. C **38** (2005) 437 [hep-ex/0407018].

[8] S. Chekanov *et al.* [ZEUS Collaboration], Eur. Phys. J. C **49** (2007) 511 [hep-ex/0608028].

[9] S. Chekanov *et al.* [ZEUS Collaboration], Phys. Lett. B **595** (2004) 86 [hep-ex/0402019].

[10] A. Gehrmann-De Ridder, T. Gehrmann and E. Poulsen, Phys. Rev. Lett. **96** (2006) 132002 [hep-ph/0601073].

[11] A. Gehrmann-De Ridder, T. Gehrmann and E. Poulsen, Eur. Phys. J. C **47** (2006) 395 [hep-ph/0604030].

[12] T. Sjöstrand *et al.*, PYTHIA 6.2 Physics and Manual (Version 6.224 is used) [hep-ph/0108264].

[13] H. Jung, Comput. Phys. Commun. **86** (1995) 147 (Version 3.1 is used).
(see also http://www.desy.de/ jung/rapgap.html).

[14] A. Gehrmann-De Ridder, G. Kramer and H. Spiesberger, Nucl. Phys. B **578** (2000) 326 [hep-ph/0003082].

[15] I. Abt *et al.*, Nucl. Instr. and Meth. **A 386** (1997) 310; ibid, 348.

[16] B. Andrieu *et al.* [H1 Calorimeter Group], Nucl. Instrum. Meth. A **336** (1993) 460.

[17] B. Andrieu *et al.* [H1 Calorimeter Group], Nucl. Instrum. Meth. A **350** (1994) 57.

[18] B. Andrieu *et al.* [H1 Calorimeter Group], Nucl. Instrum. Meth. A **336** (1993) 499.

[19] R. D. Appuhn *et al.*, Nucl. Instrum. Meth. A **386** (1997) 397.

[20] T. Wolff *et al.*, Nucl. Instrum. Meth. A **323** (1992) 537.

[21] A. Baird *et al.*, Nucl. Instrum. Meth. A **461** (2001) 461;
A. Schöning *et al.*, Nucl. Instrum. Meth. A **518** (2004) 542.

[22] K. Müller *et al.*, Nucl. Instrum. Meth. A **312**, 457 (1992).

[23] S. Eichenberger *et al.*, Nucl. Instrum. Meth. A **323**, 532 (1992).

[24] J. Becker *et al.*, submitted to Nucl.Instrum.Meth.A, physics/0701002.

[25] M. Bengtsson and T. Sjostrand, Z. Phys. C **37** (1988) 465.

[26] B. Andersson *et al.*, Phys. Rept. **97** (1983) 31.

[27] T. Sjöstrand, Comput. Phys. Commun. **82** (1994) 74.

[28] J. Pumplin *et al.*, JHEP **0207** (2002) 012 [hep-ph/0201195].

[29] G. Corcella *et al.*, HERWIG 6.5 Release Note **135** (2001) 128, [hep-ph/0210213] (Version 6.505 is used).

[30] GEANT 3, R. Brun *et al.*, CERN_DD/EE/84-1.

[31] C. Adloff *et al.* [H1 Collaboration], Eur. Phys. J. C **21** (2001) 33 [hep-ex/0012053].

[32] E. W. N. Glover and A. G. Morgan, Z. Phys. C **62** (1994) 311.

[33] D. Buskulic *et al.* [ALEPH Collaboration], Z. Phys. C **69** (1996) 365.

[34] S. D. Ellis and D. E. Soper, Phys. Rev. D **48** (1993) 3160 [hep-ph/9305266].

[35] C. Schmitz, Ph.D. Thesis Zürich University, 2007, in preparation, to be made available at http://www-h1.desy.de/publications/theses_list.html.

[36] S. Bentvelsen *et al.*, Proceedings of the Workshop "Physics at HERA", vol.1, eds. W. Buchmüller, G. Ingelman, DESY (1992) 23;
C. Hoeger, ibid.,43.

[37] C. Adloff *et al.* [H1 Collaboration], Eur. Phys. J. C **13** (2000) 609 [hep-ex/9908059].

[38] K. Koller *et al.*, Z. Phys. C **6**, 131 (1980).

[39] M. Glück *et al.*, Phys. Rev. Lett. **73** (1994) 388.

[40] K. Ackerstaff *et al.* [OPAL Collaboration], Eur. Phys. J. C **2** (1998) 39 [hep-ex/9708020].

[41] L. Bourhis, M. Fontannaz and J. P. Guillet, Eur. Phys. J. C **2** (1998) 529 [hep-ph/9704447].

Isolated Photon Cross Section Phase Space	
Inclusive cross section	$3 < E_T^\gamma < 10$ GeV $-1.2 < \eta^\gamma < 1.8$ $z = E_T^\gamma / E_T^{photon-jet} > 0.9$ $E'_e > 10$ GeV $153 < \theta_e < 177°$ $4 < Q^2 < 150$ GeV^2 $W_X > 50$ GeV $y > 0.05$ $\sqrt{s} = 319$ GeV
Jet definition	k_T algorithm with P_T-weighted recombination scheme [34], $R_0 = 1$ $P_T^{jet} > 2.5$ GeV $-1.0 < \eta^{jet} < 2.1$

Table 1: Phase space region in which isolated prompt photon cross sections are measured together with the definition of jets. Kinematics is defined in the H1 laboratory frame.

H1 Inclusive Isolated Photon Cross Sections					
E_T^γ [GeV]		$d\sigma/dE_T^\gamma$ [pb/GeV]	stat.	syst.	f_{had}
3.0	4.0	16.98	± 1.20	$^{+2.79}_{-2.61}$	0.78
4.0	6.0	10.51	± 0.47	$^{+1.50}_{-1.86}$	0.89
6.0	10.0	3.08	± 0.20	$^{+0.46}_{-0.60}$	0.98
η^γ		$d\sigma/d\eta^\gamma$ [pb]	stat.	syst.	f_{had}
-1.2	-0.6	26.15	± 1.67	$^{+3.60}_{-4.16}$	0.92
-0.6	0.2	20.69	± 1.34	$^{+3.53}_{-3.73}$	0.85
0.2	0.9	15.83	± 0.93	$^{+1.97}_{-3.25}$	0.81
0.9	1.4	9.57	± 0.87	$^{+1.99}_{-2.00}$	0.80
1.4	1.8	5.50	± 1.15	$^{+1.04}_{-1.75}$	0.80
Q^2 [GeV^2]		$d\sigma/dQ^2$ [pb/GeV^2]	stat.	syst.	f_{had}
4.0	10.0	2.48	± 0.21	$^{+0.34}_{-0.41}$	0.87
10.0	20.0	1.17	± 0.07	$^{+0.19}_{-0.21}$	0.83
20.0	40.0	0.52	± 0.03	$^{+0.07}_{-0.10}$	0.81
40.0	80.0	0.235	± 0.013	$^{+0.033}_{-0.048}$	0.83
80.0	150.	0.063	± 0.006	$^{+0.009}_{-0.012}$	0.87

Table 2: Differential cross sections for inclusive isolated photon production in the kinematic range specified in table 1. f_{had} denotes the hadronisation correction factor applied to the LO calculation.

H1 Inclusive Isolated Photon Cross Sections					
E_T^γ [GeV]		$d\sigma/dE_T^\gamma$ [pb/GeV]	stat.	syst.	f_{had}
$-1.2 < \eta^\gamma < -0.6$					
3.0	4.0	4.86	± 0.67	$^{+0.88}_{-0.63}$	0.86
4.0	6.0	3.46	± 0.28	$^{+0.48}_{-0.66}$	0.96
6.0	10.0	0.98	± 0.12	$^{+0.13}_{-0.23}$	1.00
$-0.6 < \eta^\gamma < 0.2$					
3.0	4.0	5.81	± 0.75	$^{+1.27}_{-1.20}$	0.76
4.0	6.0	3.20	± 0.28	$^{+0.56}_{-0.64}$	0.88
6.0	10.0	1.09	± 0.13	$^{+0.15}_{-0.16}$	0.99
$0.2 < \eta^\gamma < 0.9$					
3.0	4.0	3.94	± 0.51	$^{+0.59}_{-0.72}$	0.72
4.0	6.0	2.39	± 0.16	$^{+0.28}_{-0.51}$	0.84
6.0	10.0	0.59	± 0.06	$^{+0.09}_{-0.14}$	0.96
$0.9 < \eta^\gamma < 1.4$					
3.0	4.0	1.66	± 0.31	$^{+0.22}_{-0.31}$	0.69
4.0	6.0	0.82	± 0.12	$^{+0.21}_{-0.16}$	0.82
6.0	10.0	0.37	± 0.05	$^{+0.10}_{-0.09}$	0.96
$1.4 < \eta^\gamma < 1.8$					
3.0	4.0	0.72	± 0.28	$^{+0.23}_{-0.21}$	0.70
4.0	6.0	0.64	± 0.16	$^{+0.09}_{-0.22}$	0.81
6.0	10.0	0.049	± 0.045	$^{+0.009}_{-0.016}$	0.94

Table 3: Differential cross sections for inclusive isolated photon production $d\sigma/dE_T^\gamma$ in different η^γ bins, corresponding to the wheel structure of the LAr calorimeter (see text). The kinematic region is defined in table 1. f_{had} denotes the hadronisation correction factor applied to the LO calculation.

H1 Inclusive Isolated Photon Cross Sections for $Q^2 > 40$ GeV^2					
E_T^γ [GeV]		$d\sigma/dE_T^\gamma$ [pb/GeV]	stat.	syst.	f_{had}
3.0	4.0	3.70	±0.39	$^{+0.63}_{-0.58}$	0.80
4.0	6.0	2.53	±0.23	$^{+0.43}_{-0.43}$	0.87
6.0	10.0	1.30	±0.15	$^{+0.19}_{-0.27}$	0.96
η^γ		$d\sigma/d\eta^\gamma$ [pb]	stat.	syst.	f_{had}
-1.2	-0.6	9.61	±1.00	$^{+1.48}_{-2.02}$	0.97
-0.6	0.2	5.13	±0.59	$^{+0.92}_{-0.97}$	0.86
0.2	0.9	3.49	±0.32	$^{+0.45}_{-0.72}$	0.78
0.9	1.4	2.37	±0.33	$^{+0.49}_{-0.47}$	0.76
1.4	1.8	1.12	±0.51	$^{+0.21}_{-0.34}$	0.73

Table 4: Differential cross sections for inclusive isolated photon production in the kinematic range specified in table 1 and $40 < Q^2 < 150$ GeV^2. f_{had} denotes the hadronisation correction factor applied to the LO calculation.

		H1 Photon plus no-Jets				H1 Photon plus Jet			
E_T^γ [GeV]		$d\sigma/dE_T^\gamma$ [pb/GeV]	stat.	syst.	f_{had}	$d\sigma/dE_T^\gamma$ [pb/GeV]	stat.	syst.	f_{had}
3.0	4.0	8.10	±0.93	$^{+1.82}_{-1.48}$	0.75	8.85	±0.70	$^{+1.37}_{-1.38}$	0.82
4.0	6.0	3.79	±0.29	$^{+0.69}_{-0.77}$	0.91	6.65	±0.35	$^{+0.92}_{-1.15}$	0.89
6.0	10.0	0.77	±0.10	$^{+0.14}_{-0.18}$	1.10	2.35	±0.17	$^{+0.35}_{-0.46}$	0.97
η^γ		$d\sigma/d\eta^\gamma$ [pb]	stat.	syst.	f_{had}	$d\sigma/d\eta^\gamma$ [pb]	stat.	syst.	f_{had}
−1.2	−0.6	9.30	±1.07	$^{+1.53}_{-1.72}$	0.88	16.61	±1.20	$^{+2.67}_{-2.64}$	0.97
−0.6	0.2	8.46	±0.95	$^{+1.73}_{-1.84}$	0.81	12.32	±0.90	$^{+2.15}_{-2.19}$	0.88
0.2	0.9	5.98	±0.71	$^{+1.16}_{-1.34}$	0.82	9.94	±0.59	$^{+1.16}_{-2.03}$	0.81
0.9	1.4	2.57	±0.47	$^{+0.64}_{-0.61}$	0.85	6.99	±0.73	$^{+1.38}_{-1.40}$	0.79
1.4	1.8	2.40	±0.73	$^{+0.78}_{-0.74}$	0.97	3.22	±0.85	$^{+0.61}_{-1.01}$	0.71
Q^2 [GeV^2]		$d\sigma/dQ^2$ [pb/GeV^2]	stat.	syst.	f_{had}	$d\sigma/dQ^2$ [pb/GeV^2]	stat.	syst.	f_{had}
4.0	10.0	1.09	±0.16	$^{+0.21}_{-0.22}$	0.96	1.39	±0.13	$^{+0.20}_{-0.22}$	0.85
10.0	20.0	0.44	±0.05	$^{+0.09}_{-0.09}$	0.88	0.76	±0.05	$^{+0.11}_{-0.14}$	0.85
20.0	40.0	0.21	±0.02	$^{+0.04}_{-0.05}$	0.93	0.31	±0.02	$^{+0.04}_{-0.06}$	0.82
40.0	80.0	0.071	±0.008	$^{+0.012}_{-0.017}$	1.09	0.162	±0.010	$^{+0.024}_{-0.033}$	0.86
80.0	150.	0.021	±0.004	$^{+0.005}_{-0.007}$	1.35	0.040	±0.005	$^{+0.005}_{-0.007}$	0.73

Table 5: Differential cross sections for the production of isolated photons accompanied by no or at least one hadronic jet in the kinematic range specified in table 1. f_{had} denotes the hadronisation correction factor applied to the LO and the NLO calculation.

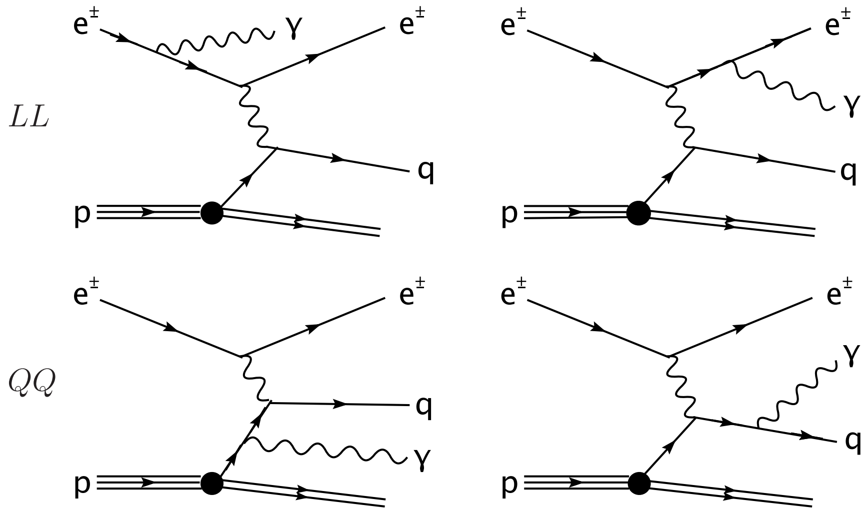

Figure 1: Leading order Feynman graphs for isolated photon production in DIS. The upper diagrams illustrate isolated photon production by radiation from the electron line (LL), while the lower diagrams correspond to production via radiation from the quark (QQ without the contribution from fragmentation).

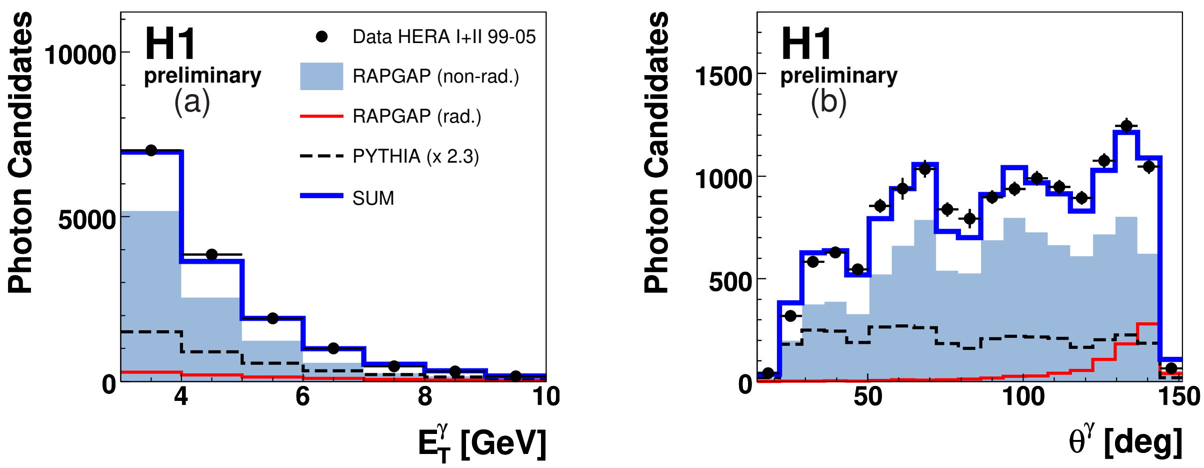

Figure 2: Distributions of (a) E_T^γ and (b) θ^γ for isolated photon candidates in the final event sample. Data are shown as points with error bars. The bold solid histogram shows the sum of the expectation from RAPGAP (non-rad.) for neutral hadron background (shaded), from PYTHIA for radiation from the quark scaled by a factor of 2.3 (dashed line) and from RAPGAP (rad.) for radiation from the electron (solid line). The unshaded area corresponds to the expected isolated photon contribution.

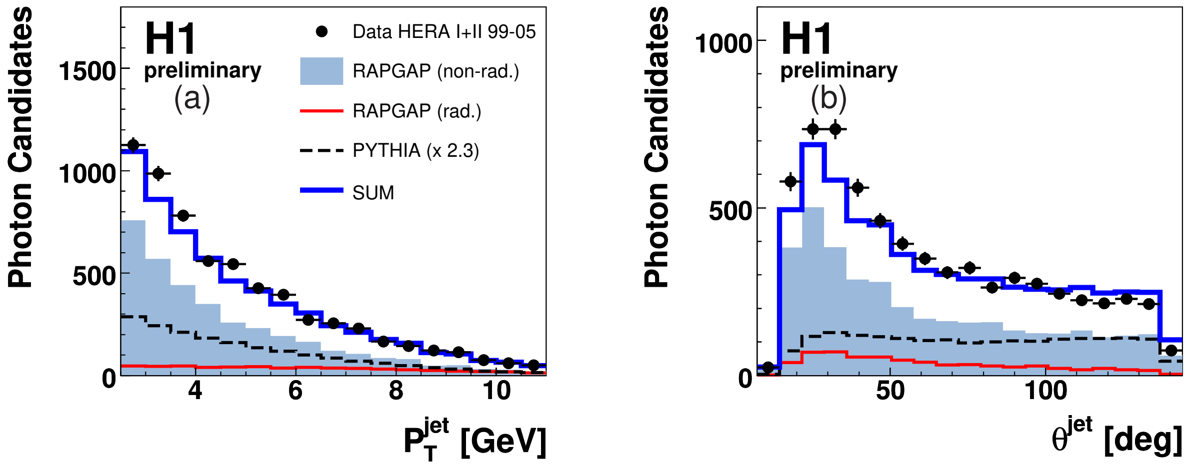

Figure 3: Distributions of (a) the transverse momentum and (b) the polar angle of the hadronic jet with the highest transverse momentum in events with an isolated photon candidate. The data are compared to the MC predictions, as described in the figure 2 caption.

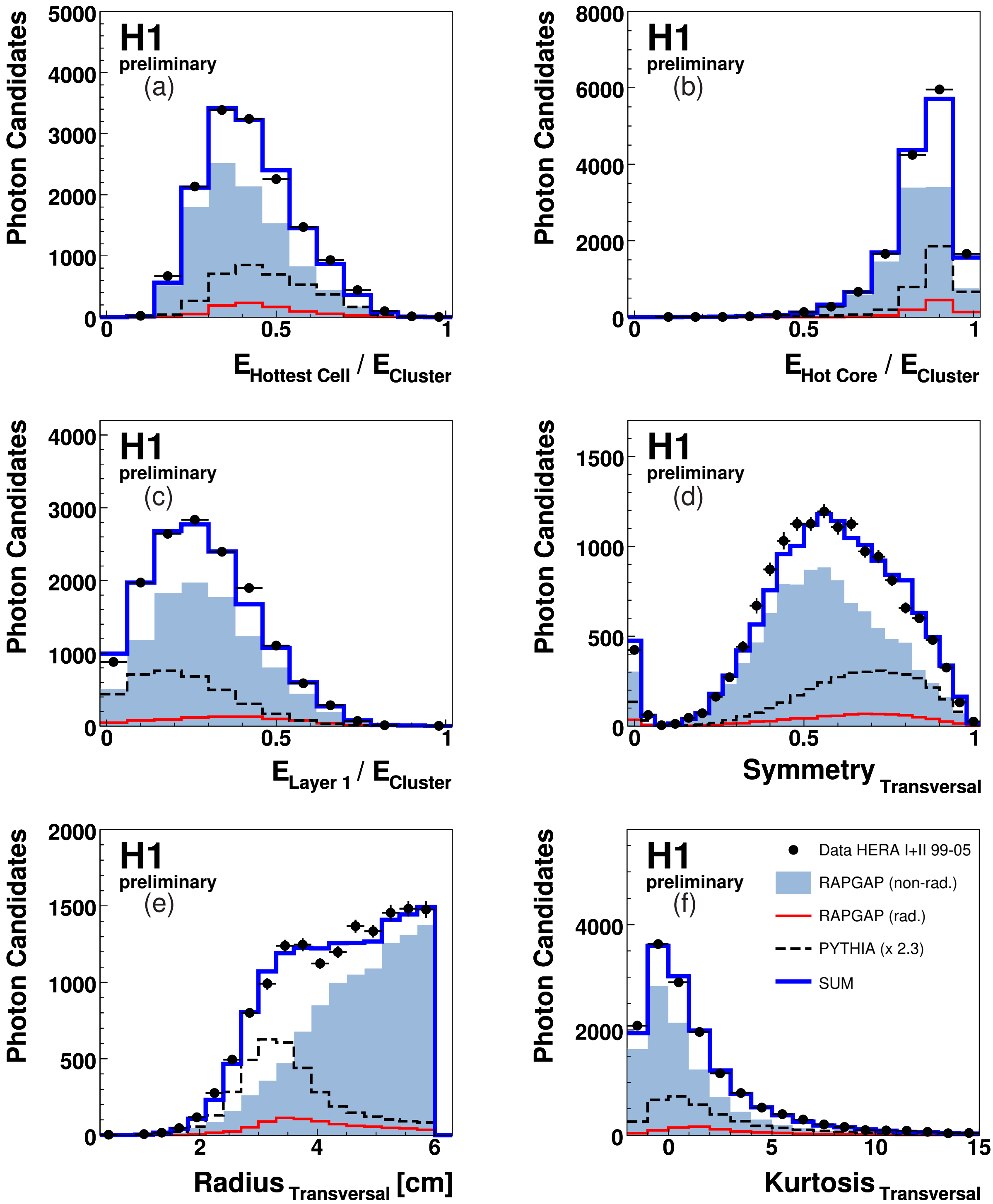

Figure 4: Distributions of the six variables that are used to define the discriminant for isolated photon identification: (a) hottest cell fraction, (b) fraction of the hot core, (c) first layer fraction, (d) transverse symmetry S_T, (e) transverse radius R_T and (f) the transverse kurtosis K_T. The data are shown with the MC predictions described in the caption to figure 2. The shape difference between RAPGAP (rad.) and PYTHIA arises from the different distributions in phase space (see figure 2b).

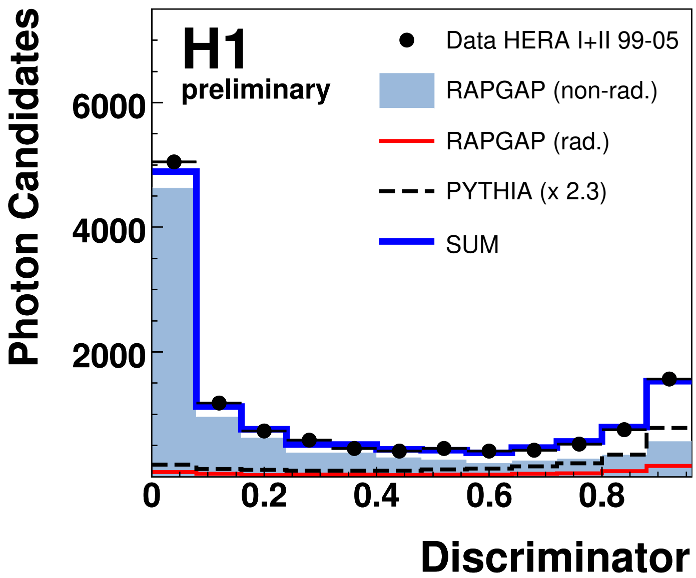

Figure 5: The distribution of the discriminator (D) used in the identification of isolated photon candidates for events that have passed the event selection. The data are compared to the MC predictions described in the figure 2 caption.

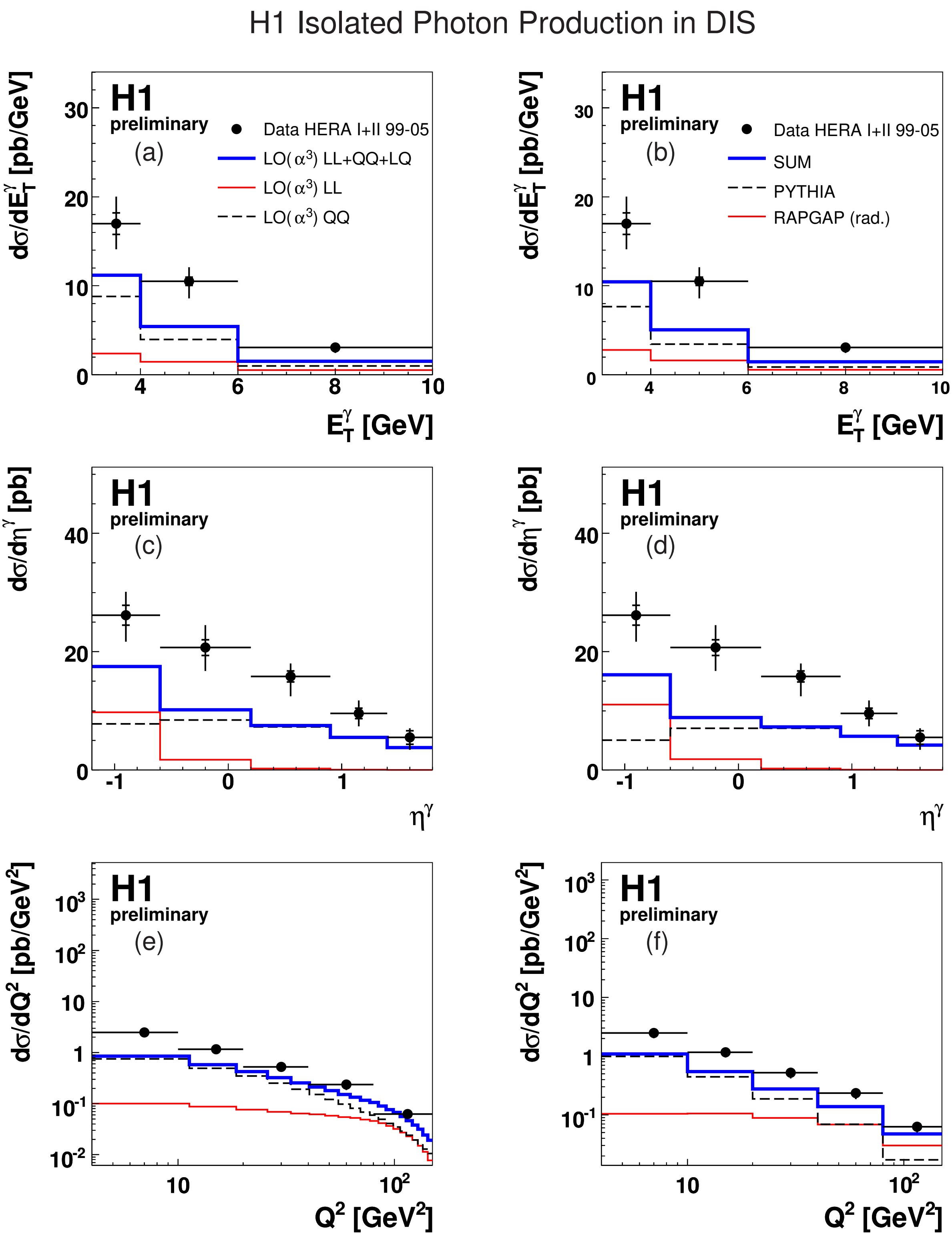

Figure 6: Differential cross sections for inclusive isolated photon production $d\sigma/dE_T^\gamma$, $d\sigma/d\eta^\gamma$, and $d\sigma/dQ^2$ in the kinematic range specified in table 1. The inner error bars on the data points indicate the statistical error, the full error bars contain in addition the systematical errors added in quadrature. The cross sections in (a, c, e) are shown together with a leading order, $\mathcal{O}(\alpha^3\alpha_s^0)$, calculation corrected for hadronisation effects, LL corresponding to radiation from the electron and QQ to radiation from the quark. The same cross sections are shown in (b, d, f) together with the prediction from PYTHIA for photon emission from the quark and from RAPGAP (rad.) for emission from the electron.

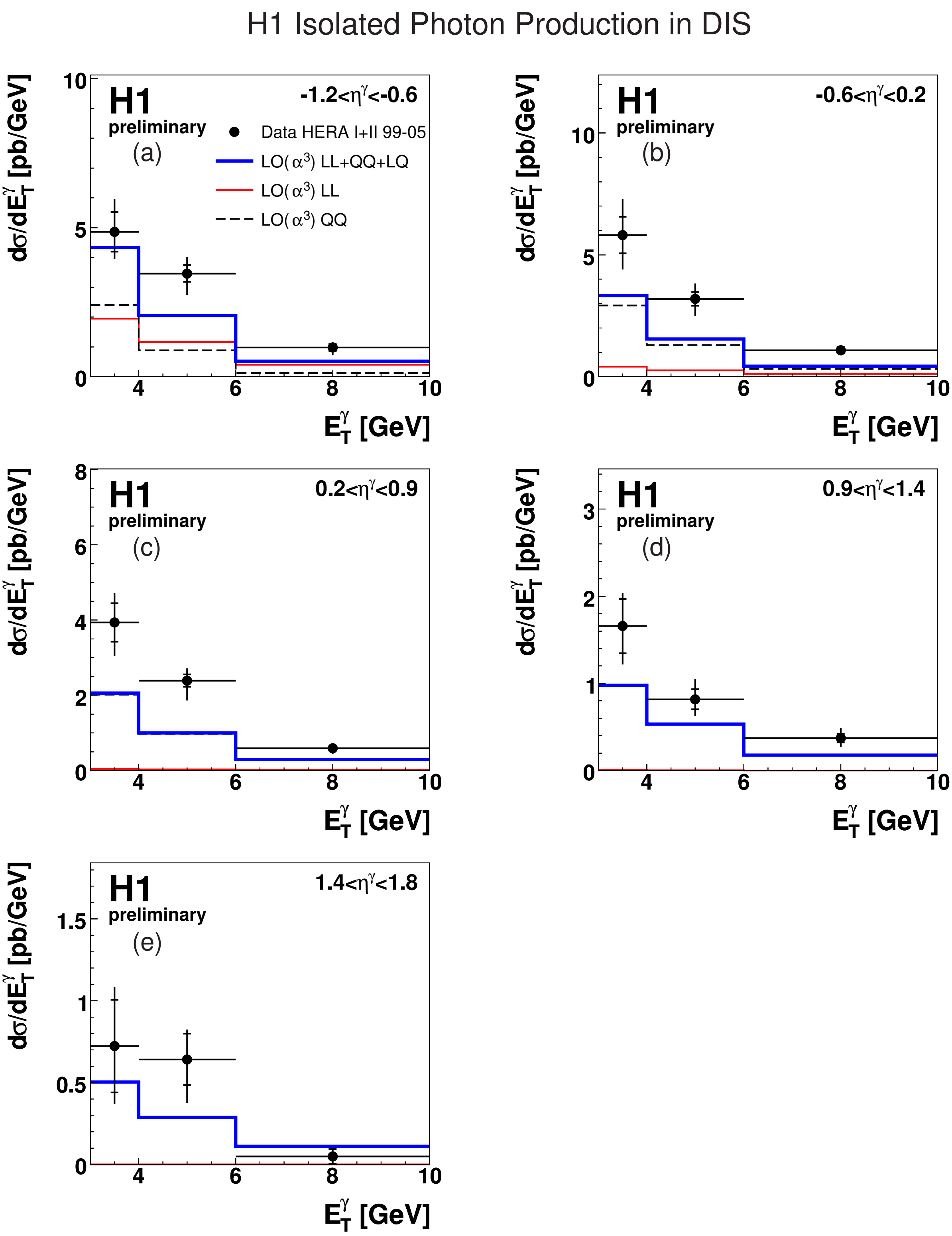

Figure 7: Differential cross sections for inclusive isolated photon production in the kinematic range specified in table 1, in η^γ bins corresponding to the wheel structure of the LAr calorimeter (see text). The LL contribution is negligible for $\eta^\gamma > 0.2$. The measurements are compared to a leading order calculation, as described in the figure 6 caption.

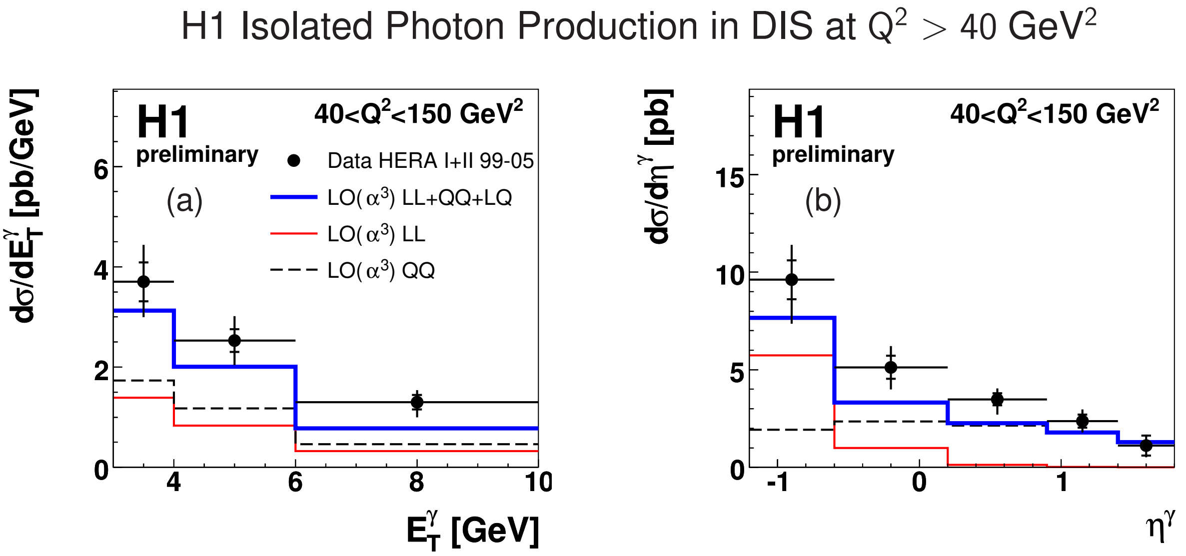

Figure 8: Differential inclusive cross sections $d\sigma/dE_T^\gamma$ (a), $d\sigma/d\eta^\gamma$ (b) for isolated photon production in the kinematic range specified in table 1 and the additional criterion $40 < Q^2 < 150$ GeV^2. The cross sections are compared to a leading order, $\mathcal{O}(\alpha^3\alpha_s^0)$, calculation as in figure 6.

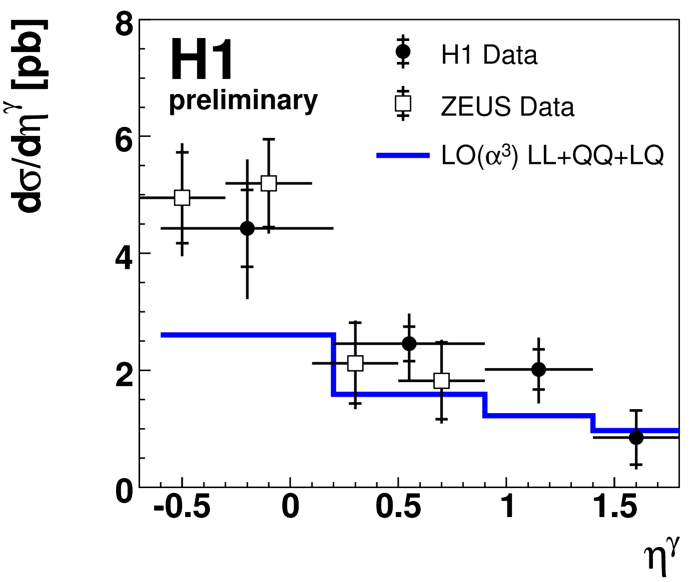

Figure 9: Differential cross sections $d\sigma/d\eta^\gamma$ for the inclusive isolated photon production in comparison to the previous measurement by ZEUS [9] for $Q^2 > 35$ GeV^2, $E'_e > 10$ GeV, $139.8 < \theta_e < 171.9°$ and $5 < E_T^\gamma < 10$ GeV. The additional condition $W_X > 50$ GeV is used in the H1 analysis only (see section 8). The cross sections are compared to a leading order, $\mathcal{O}(\alpha^3\alpha_s^0)$, calculation as in figure 6. The calculation is corrected for hadronisation effects in contrast to the comparison in [10].

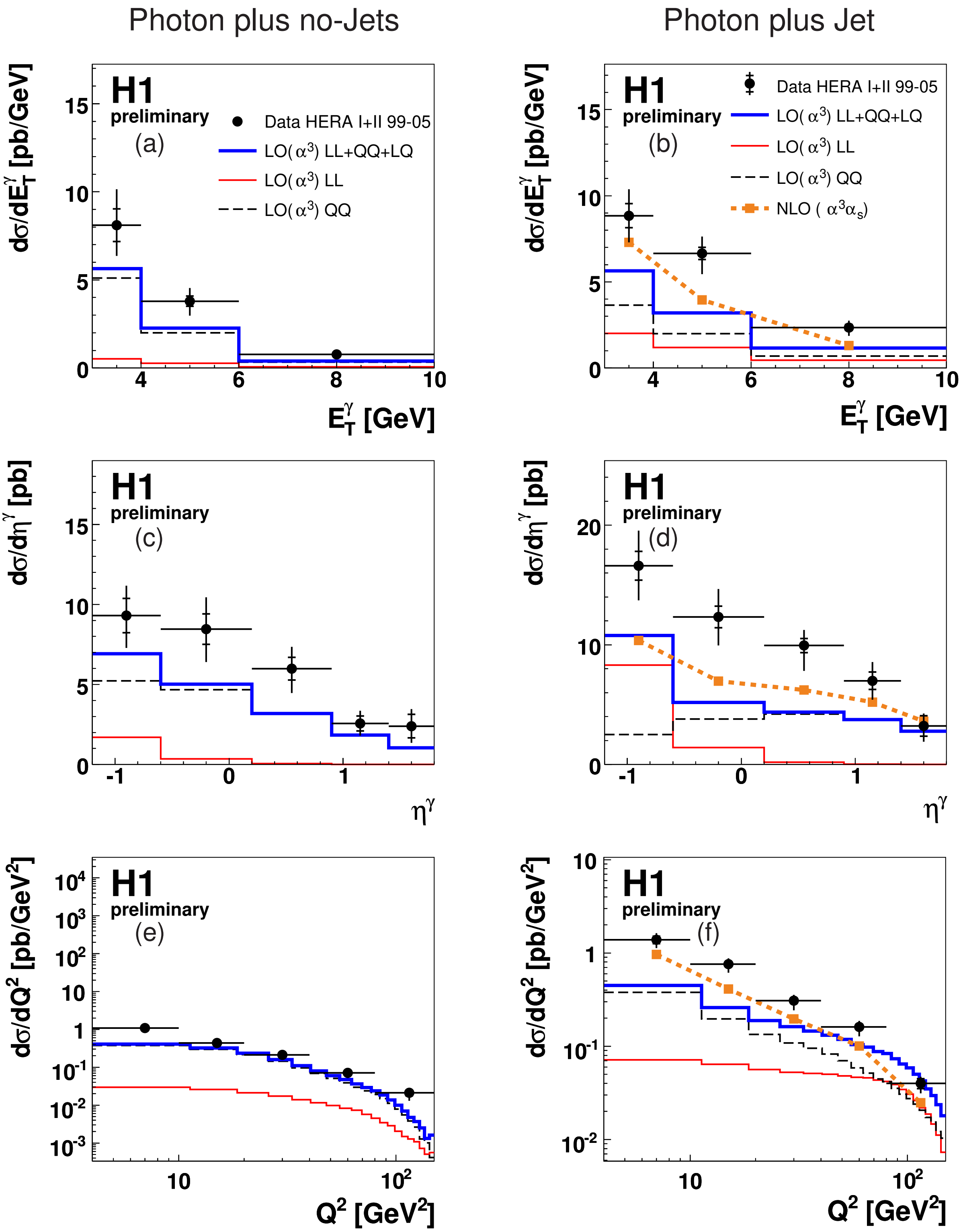

Figure 10: Differential cross sections $d\sigma/dE_T^\gamma$, $d\sigma/d\eta^\gamma$ and $d\sigma/dQ^2$ for photon plus no-jets (a, c, e), and photon plus jet (b, d, f) production in the kinematic range specified in table 1. The cross sections are compared to a leading order, $\mathcal{O}(\alpha^3\alpha_s^0)$, calculation as in figure 6. The photon plus jet sample is additionally compared to a NLO $(\alpha^3\alpha_s)$ calculation. Both, LO and NLO predictions are corrected for hadronisation effects. The points in the NLO calculation indicate the bin averaged cross section.